Effect of Mo-doping in SnO₂ thin film photoanodes for water oxidation

Farabi Bozheyev [a,b,c,*], *Eser Metin Akinoglu* [a,d], *Lihua Wu* [a], *Shuting Lou* [a], *Michael Giersig* [a,e]

[a] *International Academy of Optoelectronics at Zhaoqing, South China Normal University, Liyuan Street, 526238, Guangdong, China*
[b] *National Nanolaboratory, Al-Farabi Kazakh National University, 71 Al-Farabi Ave, 050000, Almaty, Kazakhstan*
[c] *Nazarbayev University, 53 Kabanbay Batyr St, 010000, Astana, Kazakhstan*
[d] *ARC Centre of Excellence in Exciton Science, School of Chemistry, University of Melbourne, Parkville, VIC, 3010, Australia*
[e] *Institute of Fundamental Technological Research, Polish Academy of Sciences, 02-106 Warsaw, Poland*

HIGHLIGHTS

- Increase in Mo concentration decreases the optical band gap of Mo:SnO₂ film.
- The lowest optical direct band gap of 2.7 eV is achieved for Sn/Mo = 1.5.
- $j = 0.6$ mA cm^{-2} at 0 V$_{RHE}$ and E$_{onset}$ = 0.14 V$_{RHE}$ are measured.
- 22% of incident photon to current transfer efficiency is measured at 450 nm.
- Concentration of O vacancies increases with increasing concentration of Mo.

GRAPHICAL ABSTRACT
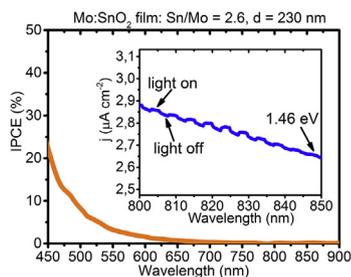
ARTICLE INFO

ABSTRACT

New semiconducting metal oxides of various compositions are of great interest for efficient solar water oxidation. In this report, Mo-doped SnO₂ (Mo:SnO₂) thin films deposited by reactive magnetron co-sputtering in the Ar and O₂ gas environment are studied. The Sn to Mo ratio in the films can be controlled by changing the O₂ partial pressure and the deposition power of the Sn and Mo targets. Increasing the Mo concentration in the film leads to the increase in the oxygen vacancy density, which limits the maximum achievable photocurrent density. The thin films exhibit a direct band gap of 2.7 eV, the maximum

* Corresponding author. International Academy of Optoelectronics at Zhaoqing, South China Normal University, Liyuan Street, 526238 Guangdong, China.
E-mail address: farabi.bozheyev@gmail.com (F. Bozheyev).

achievable photocurrent density of 0.6 mA cm^{-2} at 0 V$_{RHE}$ and the onset potential of 0.14 V$_{RHE}$. The incident photon to current transfer (IPCE) efficiency of 22% is shown at a 450 nm wavelength. The initial performance of the Mo:SnO$_2$ thin films is evaluated for solar water oxidation.

Introduction

In the last decades, semiconducting ternary metal oxides attracted much interest for solar water splitting due to their various physical and chemical properties [1–6]. These properties directly depend on the fabrication and further optimization methods, which significantly determine the main semiconductor parameters such as the band gap, light absorption, photocatalytic activity and material stability [7]. For efficient solar water splitting, the electrodes should absorb visible light efficiently to generate electron–hole pairs, which should be separated and transported to the semiconductor/electrolyte interface (SEI) to be utilized for the catalytic process [1–3,8]. Therefore, a suitable semiconducting compound is of paramount importance to address these requirements.

Among the metal oxides, BiVO$_4$ has been intensively studied in different groups demonstrating the best photoelectrochemical performance as a photoanode to date [9–12]. The efficiency of BiVO$_4$ is limited by its large band gap (2.5 eV), therefore, alternative ternary compounds are of primary significance. To achieve an efficiency as high as 20–30%, the band gap of the materials should be in the range of 1.5–1.9 eV, i.e. higher than the potential (1.23 eV) required for water splitting taking into account overpotentials [1,13]. With respect to the suitable band gap, ternary metal oxides such as Fe$_2$TiO$_5$ [14], Fe$_2$WO$_6$ [15], MnV$_2$O$_7$ [16], CuBi$_2$O$_4$ [17], and SnNb$_2$O$_6$ [18] were identified as promising materials for photoelectrochemical water splitting.

Recently, SnWO$_4$ gained attention due to its suitable band gap (1.5–1.9 eV) [19–22] and potential for photoelectrochemical water splitting [23–25]. However, its low photoactivity and instability require further theoretical and experimental efforts. A novel β-SnMoO$_4$ was studied by systematic search of known and hypothetical various compounds [26], which is a similar compound to SnWO$_4$. Herein, the density functional theory calculations established β-SnMoO$_4$ as a potential photoelectrode taking into account its band gap, band-edge positions and thermodynamic stability.

The photoelectrode optical band gap can be tuned through doping with electron donor or acceptor elements, since they create additional energy levels in the band gap. Among the elements, Mo is widely used as co-catalyst and beneficial dopant for photoanodes due to its thermal stability and unique electronic configuration. It exhibits different oxidation states (Mo^{4+} and Mo^{6+}) and suitable ionic radii (0.62 Å and 0.7 Å) to substitute Sn^{4+} (0.083 nm) in the SnO$_2$ lattice. It was shown, that Mo doping (15 at.% Mo) in SnO$_2$ nanoparticles slightly decreased the optical band gap from 3.56 eV to 3.44 eV and improved the photocatalytical properties considerably [27]. Due to the difference in the valency of Sn^{4+} and Mo^{6+} two electrons are donated to the SnO$_2$ lattice modifying its intrinsic optoelectronic properties. In this report, we aimed to study Mo-doped SnO$_2$ thin films as a photoanode material for solar water oxidation, which was not reported before to the best of our knowledge. In addition, we show an optical band gap decrease down to 2.7 eV by controlling the Mo doping in SnO$_2$. The Mo:SnO$_2$ thin films prepared by reactive magnetron co-sputtering are compositionally, structurally, optically and photoelectrochemically characterized.

Experimental section

Sample fabrication

Mo:SnO$_2$ thin films were deposited by radio-frequency (RF) reactive magnetron co-sputtering from Sn (99.99%) and Mo (99.95%) targets at room temperature. The schematic of the deposition process is shown in Fig. S1. To vary the film composition, first the oxygen partial pressure (P$_{O2}$) was varied from 0 to 0.42 Pa at a fixed Ar pressure of 0.9 Pa. The deposition time was varied from 4 min to 12 min for the preparation of various film thicknesses ranging from 200 nm to 450 nm on n-Si and fluorine doped tin oxide (FTO) substrates. To study the film crystallization, the annealing temperature was varied from room temperature up to 600 °C for 20 min in a vacuum environment inside a split tube furnace. The sample color varies with P$_{O2}$ from bluish to brown dark (Fig. S2).

Material characterization

The film structure was studied by X-ray diffraction (XRD) using a Bruker D8 Advance diffractometer (CuKα, 0.15406 nm). The film morphology and element distribution were studied by scanning electron microscopy (SEM) and energy dispersive X-ray analysis (EDX) using a Zeiss Sigma 500 and Oxford Instrument. The oxidation states of the elements and the film composition were studied by X-ray photoelectron spectroscopy (XPS) using an AlKa irradiation (1486.6 eV) using a Thermo ESCALAB 250XI system. For elemental analysis, inductively coupled plasma mass spectroscopy (ICP-MS) was performed by an Agilent ICPOES730 system. RF power was 1.5 kW, the carrier gas was argon, the plasma gas flow was 15 L/min, the auxiliary gas flow was 1 L/min, the compensation gas flow was 0.1 L/min. The detector mode and the

calibration type were axial and linear, respectively. The transflectance (TR = T + R, T − transmittance, R - reflectance) spectra of the films on FTO were measured using a UV/VIS/NIR system (PerkinElmer Lambda 1050 Spectrophotometer) inside the integrating sphere. The absorptance was determined as A = 1 − TR and the absorption coefficient was calculated as $\alpha = \frac{-\ln(TR)}{d}$, where d is the film thickness measured from cross section SEM captures.

Photoelectrochemical characterization

The current density-voltage (j-V) measurements were performed in the photoelectrochemical cell containing Mo:SnO$_2$ as a working electrode, a Pt ring as a counter electrode and an Ag/AgCl (3.5 M KCl) as a reference electrode in 0.5 M Na$_2$SO$_4$ (pH = 7) electrolyte solution using a potentiostat (Chinstrument 600E). A solar simulator AM 1.5 with an irradiation power of 100 mW cm^{-2} was used as an illumination source. The potentials measured using the Ag/AgCl (in saturated 3.5 M KCl solution, $V^0_{Ag/AgCl}$ = 0.198 V) redox potential were converted into the reversible hydrogen electrode (RHE) scale using the Nernst equation:

$$V_{RHE} = V_{Ag/AgCl} + 0.0591 \times pH + V^0_{Ag/AgCl},$$

where, $V_{Ag/AgCl}$ is the applied potential and $V^0_{Ag/AgCl}$ is the standard potential of the Ag/AgCl reference electrode.

For electric contact, a copper wire was attached to the FTO substrate using an adhesive Al sheet. The linear scan voltammetry (LSV) curves were measured at a scan rate of 50 mV s^{-1} from −0.5 to 0.7 V vs. Ag/AgCl. The diameter of the working electrode was a circle with a diameter of 1 cm. The incident photon to current efficiency (IPCE) was measured using a Xe-arc lamp combined with a monochromator (CEL-SLF 300, Fig. S3) and a long pass filter in the dark sample compartment. The IPCE was measured using the following equation:

$$IPCE(\lambda) = \frac{1240 \, (nm) \times 1.23(V) \times J_{ph}(\lambda)}{\lambda I_\lambda(\lambda)}$$

where, λ is the incident light wavelength (nm), $J_{ph}(\lambda)$ is the measured photocurrent density (mA cm^{-2}) of photoanode and $I_\lambda(\lambda)$ is the light power density (mW/cm^2) for each λ measured for front side illumination through the quartz window.

Results and discussion

Composition and morphology

The SEM image in Fig. 1a shows the morphology of the film surface with small Mo:SnO$_2$ grains formed on top of the n-Si substrate. The cross section image in the inset shows the 400 nm thick Mo:SnO$_2$ film. EDX mapping of the film surface revealed an almost homogeneous distribution of Mo, Sn and O (Fig. S4). To optimize the composition, first the P_{O2} was varied in the chamber at a constant P_{Ar}. The EDX analysis revealed that the enhancement of P_{O2} from 0 Pa to 0.32 Pa decreases the Mo concentration as can be seen from the decrease in the Mo peak intensity (Fig. S5). The reason for that could be a faster
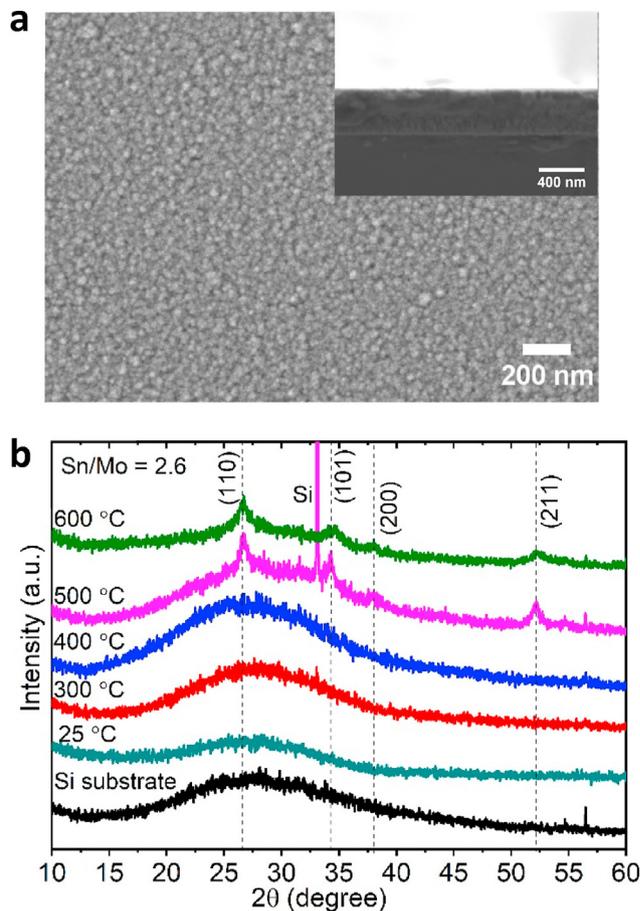
Fig. 1 − (a) SEM images of the surface and the cross section (inset) of a Mo:SnO$_2$ film (Sn/Mo = 2.6) crystallized at 300 °C in vacuum on a n-Si substrate. (b) XRD patterns of Mo:SnO$_2$ (Sn/Mo = 2.6) thin films on n-Si substrates as a function of the temperature.

oxidation rate than that of a sputtering rate of the Mo target. Further, the Sn/Mo ratio was tuned by power variation at the Mo target at a constant power of the Sn target at a power of 100 W. To measure the Sn/Mo ratio precisely, the ICP-MS measurements were carried out, where the variation of the Mo power (50 W, 70 W, 85 W and 100 W) led to 2.8, 2.6, 2.2 and 1.5 for Sn/Mo ratios, i.e. 10, 11, 13 and 18 at.% of Mo concentration, respectively (Table 1). The morphology of the samples is almost similar independent on the Sn/Mo ratio (Fig. S6).

Table 1 − The relation between the Sn/Mo ratio, thickness, optical band gap and photocurrent density for Mo:SnO$_2$ films as a function of Sn power.

Sn power (W)	Sn/Mo ratio	at. % Mo	Film thickness (nm)	$(\alpha h\nu)^2$ (eV)	j at 1.23 V_{RHE} (mA cm^{-2})
100	1.5	18	400	2.7	0.04
85	2.2	13	400	3	0.16
70	2.6	11	360	3.5	0.2
50	2.8	10	280	3.65	0.046
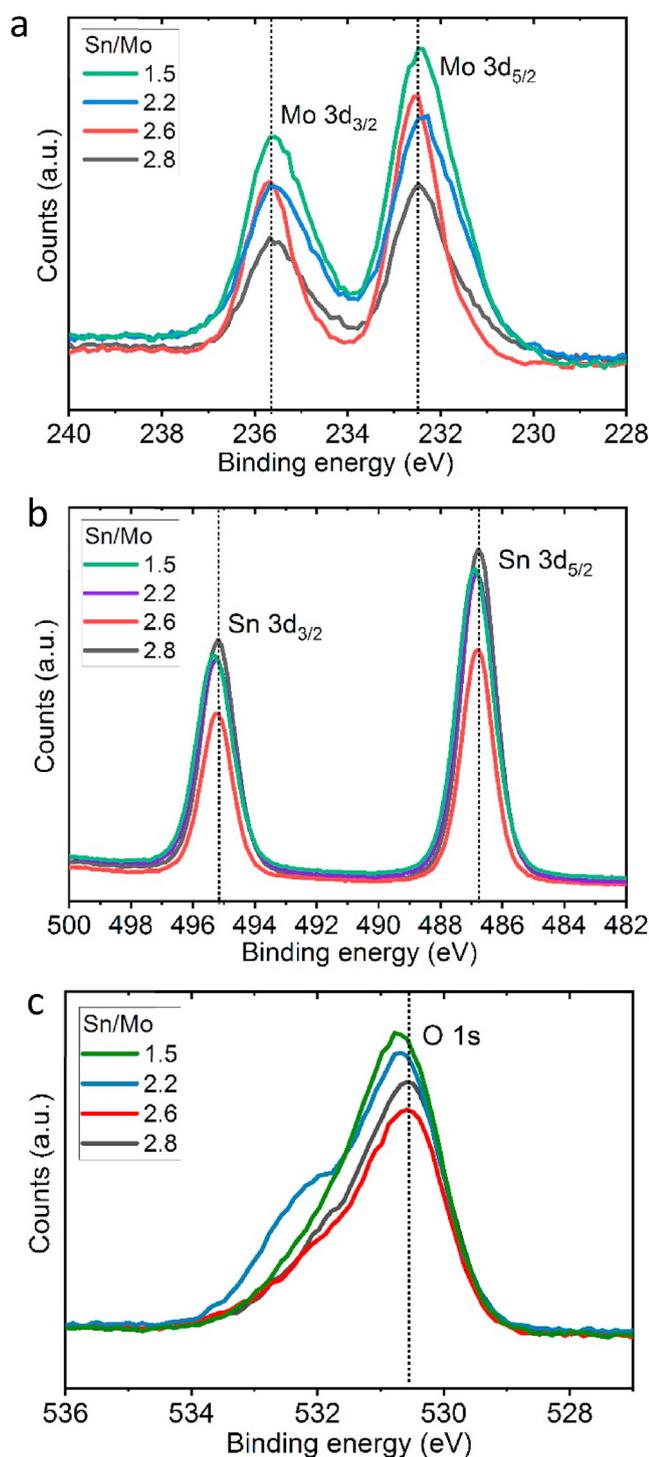
Fig. 2 – XPS spectra for (a) Mo 3d, (b) Sn 3d, (c) O 1s for Mo:SnO$_2$ films as a function of Sn/Mo ratio.

Structural and phase composition

The structure and phase composition of the as-prepared and annealed films were studied by XRD (Fig. 1b). The as-prepared and annealed films up to 400 °C do not exhibit any diffraction peaks implying the presence of an amorphous phase. The

most pronounced peaks are attributed to the Si substrate. The ionic radius of Mo is close to W, and here one should expect the crystallization of the orthorhombic phase similar to SnWO$_4$ (PDF 01-070-1049) [28]. In our previous report, SnWO$_4$ films successfully crystallized at 600 °C [29]. Here, annealing of the films up to 600 °C leads to the crystallization of the SnO$_2$ phase and no characteristic diffraction peaks for a tin molybdate phase were observed. Increase in the Mo concentration inhibits the film crystallization. The widening of the full width at half maximums (FWHMs) of the (110), (101), (200) and (210) peaks of SnO$_2$ crystallized at 600 °C points to the decrease in the grain size (Fig. S7). SnO$_2$ prepared by precipitation techniques demonstrated an amorphous phase at 400 °C and subsequent crystallization at 600 °C in previous reports [30]. This was due to segregation and volatilization of MoO$_3$ at temperatures higher than 600 °C [31]. In such process, Mo is not able to find the space within the rutile matrix of SnO$_2$ causing lattice damage and structural disorder.

All films annealed at 300 °C have not shown any diffraction peaks presuming the amorphous structure. However, recently, a phase transition from the columbite (C–SnO$_2$) to the rutile (R–SnO$_2$) structure in the temperature range of 100–300 °C was shown [32]. Here, the diffraction peaks were merged as a wide diffraction shoulder due to the finite size of the crystallites known as the Debye-Scherrer broadening. In addition, our previous report also confirmed small SnO$_2$ crystallites in the amorphous matrix in the as-prepared tin tungstate film by TEM measurements [29]. As a result, the film annealed at 300 °C is considered as a combination of amorphous, columbite and rutile structures.

It is well known, that the morphology, crystal structure and surface disorder for tin-molybdenum oxide depends on the calcination conditions and Mo-concentration [30]. For instance, a Mo-deficient (at. 1%) tin-molybdenum oxide calcinated at 400 °C exposed much crystallographic order with a large amount of planar defects. While the Mo-rich (at. 20%) tin-molybdenum oxide calcinated at 400 °C exhibited a substantial amount of amorphous nanoparticles and lattice disorder. These observations indicate that Mo inhibits the crystal growth of tin-molybdenum oxide. Despite crystallization, an increase in the temperature up to ca. 900–1000 °C led to much surface disorder [30]. The results for the Mo:SnO$_2$ films prepared at a different Mo concentration correspond well with the observed facts.

The XPS analysis reveals that the increase in the Mo concentration from 10 to 18 at. % enhances the intensity of the Mo 3d$_{5/2}$ and Mo 3d$_{3/2}$ peaks and negatively shifts their position from 232.50 eV and 235.68 eV to 232.36 eV and 235.54 eV ($\Delta E = 0.14$ eV) due to the reduction of Mo (Fig. 2a). The positions of the Mo 3d peaks corresponds to a MoO$_3$ phase in the film [33]. Whereas the Sn 3d$_{5/2}$ and 3d$_{3/2}$ peaks at 486.78 eV and 495.18 eV positively shift to 486.88 eV and 494.28 eV ($\Delta E = 0.1$ eV) indicating the oxidation of the Sn (Fig. 2b). The reason for that is the larger electronegativity of Mo (2.16) in respect to Sn (1.96) according to the Pauling scale. The O 1s peak maximum shifts from 530.58 eV to 530.78 eV ($\Delta E = 0.2$ eV) with increasing Mo concentration due to generated oxygen vacancies (Fig. 2c), which are discussed in detail below.

Optical properties

The absorption spectra as a function of the photon energy for the Mo:SnO$_2$ films with varying composition are presented in Fig. 3a. Indeed, Mo-doping decreases the optical direct band gap of the film from 3.65 to 2.7 eV (see Tauc plots in Fig. S8), due to the creation of the additional energy levels in the band gap of SnO$_2$. The highest absorption is achieved for Sn/Mo ratio at 1.5, however, the higher concentration of Sn compared to that of Mo in the film, leads to the preferential formation of the SnO$_2$ phase. Therefore, the absorption edge is shifted to the higher energy site due to the wide band gap of SnO$_2$ of about 3.5 eV [34]. The maximum absorption coefficient of the films reaches 0.23×10^5 cm^{-1} (Fig. 3b), which is less than that of our reported values for tin tungstate films (0.65×10^5 cm^{-1}) [29].

PEC performance

The photoelectrochemical activity of the Mo:SnO$_2$ films prepared at Sn/Mo of 2.6 as a function of the temperature is shown in Fig. 4a and Fig. S9. The photocurrent density at 1.23 V$_{RHE}$ considerably increases from 0.025 to 0.2 mA cm^{-2} as the temperature increases from room to 300 °C. Such increase could be due to the structuration of the C−SnO$_2$ crystallites in the film. The temperature increase up to 400 °C leads to the recrystallization of the R−SnO$_2$ and, therefore, decrease of the photocurrent density. This trend shows how the phase transfer from C−SnO$_2$ to R−SnO$_2$ determines the value of the photocurrent density.

The photoactivity of the films was studied as a function of the Sn/Mo ratio as well as the film thickness. The optimum composition and film thickness are Sn/Mo = 2.6 and 230 nm, where the films with the thicknesses of 180 and 370 nm exhibited lower photoactivity (Fig. 4b). This could be due to the different diffusion lengths in the films attributed to the relation of the light absorption, charge carrier generation and bulk recombination processes. The Sn/Mo ratios at 1.5 and 2.4 demonstrated lower photocurrent densities than that of 2.6 (Fig. S10). The reason for that is that a bigger Mo concentration creates ionized defects in the film structure and scatters the excited charge carriers. To see a reproducible dependence of the photocurrent density on the Sn/Mo ratio, different thicknesses corresponding to 4 min, 8 min and 12 min deposition time were investigated. All curves confirm a similar dependence pointing at the maximum photocurrent density at Sn/Mo ratio of 2.6 (Fig. 5). The dependence of the photocurrent density on the film parameters are summarized in Table 1. The onset potential for the film 0.14 V$_{RHE}$ (Fig. S11) is more positive than the reported value at −0.1 V$_{RHE}$ for SnWO$_4$ [25,26], which determines the flat-band potential.

Quantum efficiency

The incident photon to current efficiency (IPCE) was measured for the Mo:SnO$_2$ (Sn/Mo = 2.6, d = 230 nm) exhibiting the highest photocurrent density at 1.23 V$_{RHE}$ (Fig. 4b and c). The IPCE signal is significantly increased with the decreasing wavelength consistent with the results of the absorption spectra (Fig. 3a). The maximum IPCE of 22% at

450 nm is achieved, which is the first reported value up to date for Mo:SnO$_2$ thin films. This value is about 2 times higher than that of the reported highest values for SnWO$_4$ [29]. The inset in Fig. 4c shows the photocurrent density upon chopped light illumination as a function of the wavelength. The photoactivity of the Mo:SnO$_2$ quenches at $\lambda = 850$ nm ($E_g = 1.46$ eV), which is rather less than the optical band gap of 2.7 eV determined from Tauc plot (Fig. S6). Such photoactivity at energies less than the band gap of the Mo:SnO$_2$ is due to the energy levels in the band gap created by Mo impurities.

PEC stability

Stability of the optimized 230 nm thick Mo:SnO$_2$ photoanode as a function of time was measured at 1.23 V$_{RHE}$ upon illumination in 0.5 M Na$_2$SO$_4$ electrolyte (Fig. 4d). The photocurrent density gradually drops from 0.8 to 0.016 mA cm^{-2} at 0 V$_{RHE}$ during 1 h due to the formation of tin sulfate SnSO$_4$ and Mo(SO$_4$)$_3$, which block the charge transfer to the electrolyte. One can see, that the dark current from the beginning totally drops after 400 s, indicating the reduction of the sample
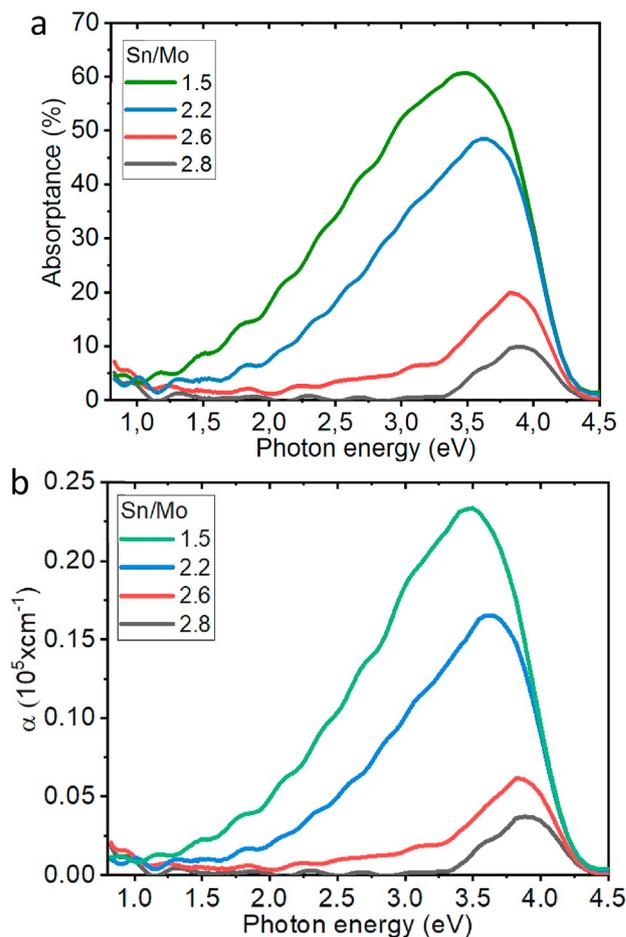
Fig. 3 − (a) Absorption spectra and (b) absorption coefficient as a function of the photon energy for the Mo:SnO$_2$ films on FTO substrate prepared at different Sn/Mo ratio and annealed at 300 °C in vacuum.
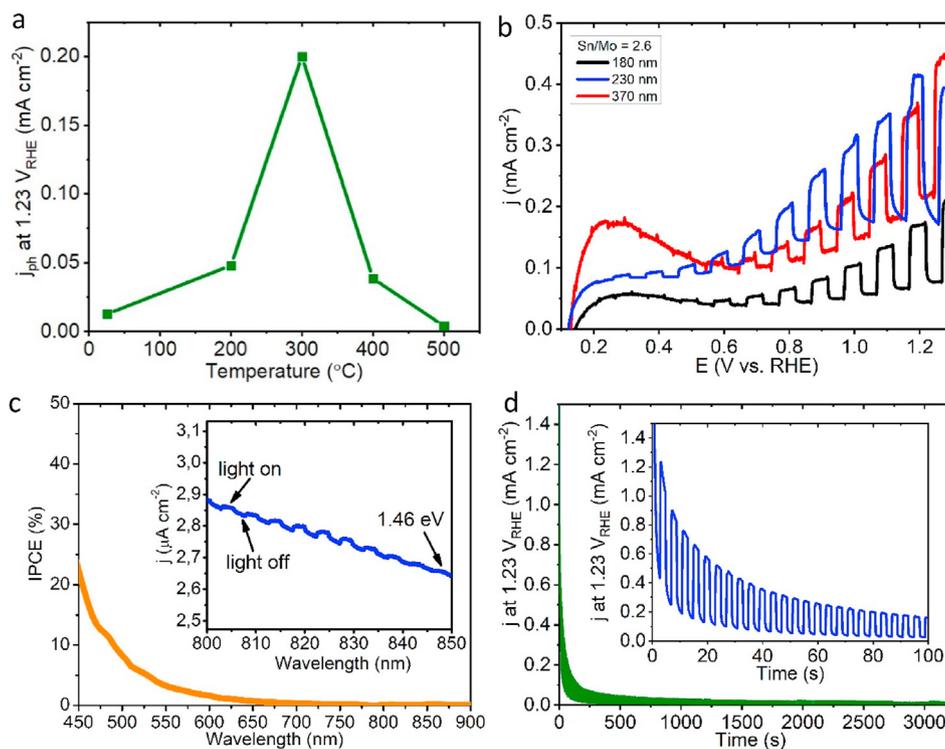
Fig. 4 – (a) Photocurrent density versus time at 1.23 V_{RHE} for Mo:SnO$_2$ films (Sn/Mo = 2.6) crystallized at different temperatures in 0.5 M Na$_2$SO$_4$ electrolyte upon chopped AM 1.5 illumination. (b) Linear scanning voltammetry (LSV) curves for Mo:SnO$_2$ photoanodes crystallized at 300 °C produced as a function of the film thickness. (c) Incident photon to current transfer efficiency (IPCE) versus the wavelength for a 370 nm thick Mo:SnO$_2$ film at 1.23 V_{RHE} in 0.5 M Na$_2$SO$_4$ solution. The inset shows that the film is photoactive up to 850 nm (E_g = 1.46 eV) upon chopped light illumination. (d) Photocurrent density versus time at 1.23 V_{RHE} for a 230 nm thick Mo:SnO$_2$ film in 0.5 M Na$_2$SO$_4$ electrolyte upon chopped AM 1.5 illumination. The inset shows the change in the initial photocurrent density.

surface. As a result, the Sn 3d$_{5/2}$ and 3d$_{3/2}$ peaks at 486.8 eV and 495.22 eV shift to 486.46 eV and 494.87 eV (Fig. 6a), at the same time Mo 3d$_{5/2}$ and 3d$_{3/2}$ peaks at 232.58 eV and 235.78 eV shift to 232.38 eV and 235.58 eV (Fig. 6b), i.e. to the lower energy. This observation is in contrast to our previously reported SnWO$_4$ film, where it was oxidized to SnO$_2$ and WO$_3$ after PEC testing [29]. During the photoelectrochemical process, the proposed next reaction steps at the interface are:

$$2SnO_2 + SO_4^{2-} + 2h^+ \rightarrow 2SnSO_4 \quad (1)$$

$$2MoO_3 + 3SO_4^{2-} + 6h^+ \rightarrow 2Mo(SO_4)_3 + 3O_2 \quad (2)$$
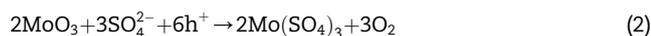
where in the reactions (1) and (2), the holes (h$^+$) generated in the film form SnSO$_4$ and Mo(SO$_4$)$_3$ reacting with SO$_4^{2-}$ at the SEI. The pristine tin molybdate only has one O 1s peak at 530.68 eV and after testing exhibits an additional peak at 531.98 eV attributed to the sulfate formation (Fig. 6c) [35]. This is also confirmed by S 2p$_{3/2}$ and 2p$_{1/2}$ peaks at 169.18 eV and 170.18 eV for the tested sample (Fig. 6d), where for pristine samples these peaks were not detected. The XPS peak
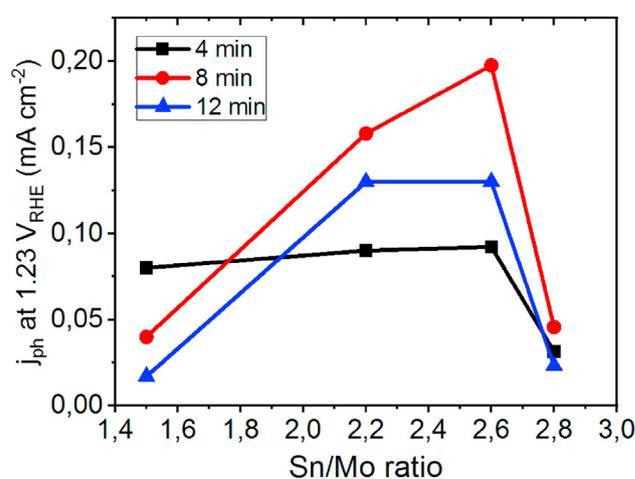
Fig. 5 – (a) Photocurrent density as a function of Sn/Mo ratio and film thickness for Mo:SnO$_2$ films crystallized at 300 °C in 0.5 M Na$_2$SO$_4$ electrolyte upon chopped AM 1.5 illumination.
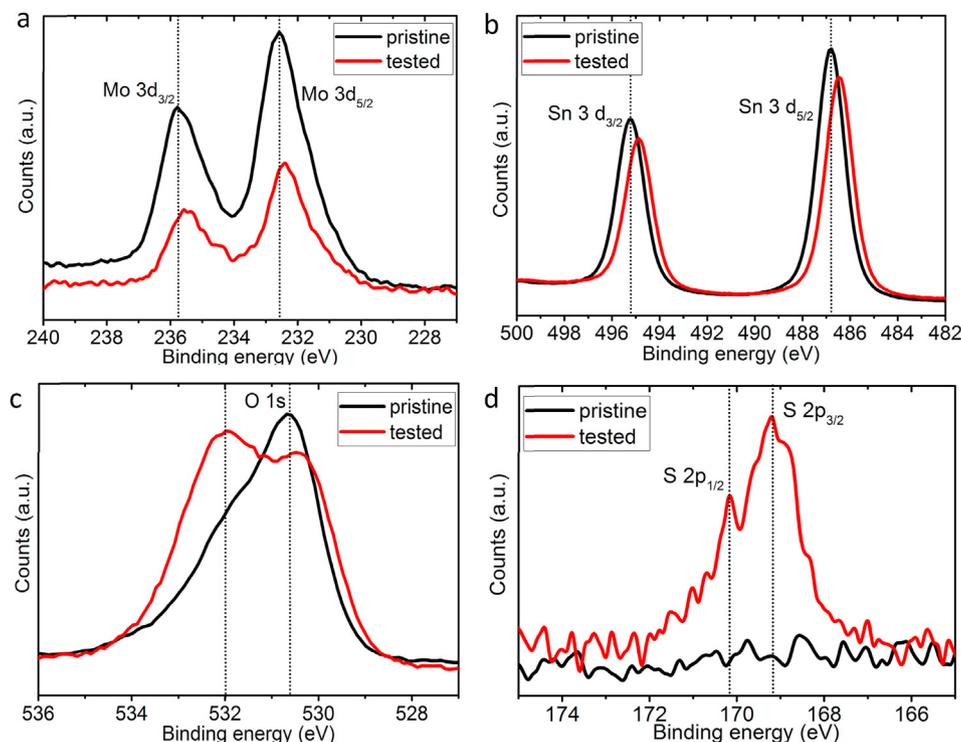
Fig. 6 — XPS spectra for (a) Mo 3d, (b) Sn 3d, (c) O 1s and (d) S 2p for Mo:SnO_2 films (Sn/Mo = 2.6) before and after PEC testing over 1 h in 0.5 M Na_2SO_4 electrolyte upon chopped AM 1.5 illumination.

positions for the $SnSO_4$ correspond well with the data reported in the literature [35]. The reduced Na species on the surface after testing are visible in Fig. S12.

Oxygen vacancies

The Mo concentration determines the photoactivity of the films as well as the oxygen vacancy in the film. The influence of the Mo doping from 10 to 18 at.% on the evolution of the O 1s regions analyzed by Gaussian fitting (Fig. S13). The O 1s curves can be represented as a convolution of three peaks centered nearly at 530.5 eV, 531.8 eV, and 532.7 eV denoted as O_L, O_M and O_H [36,37]. The O_L, O_M and O_H peaks are related to the oxygen ions combined with Sn ions, the oxygen vacancies, and the adsorbed oxygen (O_2, H_2O, CO_3). The relative proportion of oxygen vacancies was calculted as ($O_M/(O_M + O_L + O_H)$). The excess charge carriers are created by oxygen vacancy, since it represents a doubly positively charged vacancy $V_O^{\bullet\bullet}$ and two electrons: $V_O^X = \frac{1}{2}O_2 + V_O^{\bullet\bullet} + 2e^-$. The increase in the Mo concentration from 10 to 18 at.% (Sn/Mo from 2.8 to 1.5) tends to the increase the oxygen vacancy proportion from 33% to 43%. This observation is in contrast to the effective vacancy suppression with the Si doping of SnO_2 thin films, which was due to the stronger bond strength of Si—O (799.6 kJ/mol) than that of Sn—O (528 kJ/mol) [37,38]. The Mo—O (502 kJ/mol) bond strength is weaker than that of Sn—O (528 kJ/mol), therefore, during the sputtering and annealing processes the O atoms have a bigger probability to leave the SnO_2 film. In addition, Mo (0.7 Å) has a smaller atomic radius than Sn (0.83 Å), which acts as a defect and impairs the mobility of the photoexcited charge carriers.

Conclusions

Summarizing, the Mo:SnO_2 films are demonstrated as a potential photoanode material towards solar water splitting. The oxygen partial pressure (P_{O2}) determines the Sn/Mo ratio of the films in the reactive magnetron sputtering process as well as their photoelectrochemical activity. The change in the Mo power from 50 W to 100 W at constant Sn power varies Sn/Mo ratio from 2.8 to 1.5. The films with the highest Mo-concentration (18 at. %) demonstrated the lowest direct band gap of 2.7 eV. The optimized Mo:SnO_2 films (Sn/Mo = 2.6) achieved the maximum unprecedented photocurrent density of 0.6 mA cm^{-2} at 1.23 V_{RHE} without any co-catalysts, the positive onset potential at 0.14 V_{RHE} and highest IPCE of 22% at 450 nm, which indicate the benchmark of the material performance. The maximum photocurrent density is limited by an oxygen vacancy quantity, which growths with the Mo concentration. Another dopants should be further studied to passivate the oxygen vacancies to improve the performance of the SnO_2 photoanodes. The films are not stable due to the formation of $SnSO_4$ and $Mo(SO_4)_3$ layers after PEC testing, so that a suitable protection layer should be employed as the next stage.

Declaration of competing interest

The authors declare that they have no known competing financial interests or personal relationships that could have appeared to influence the work reported in this paper.

Appendix A. Supplementary data

Supplementary data to this article can be found online at https://doi.org/10.1016/j.ijhydene.2020.09.050.

REFERENCES

[1] Lee DK, Lee D, Lumley MA, Choi K-S. Progress on ternary oxide-based photoanodes for use in photoelectrochemical cells for solar water splitting. Chem Soc Rev 2019;48:2126–57.

[2] Walter MG, Warren EL, McKone JR, Boettcher SW, Mi Q, Santori EA, et al. Solar water splitting cells. Chem Rev 2010;110:6446–73.

[3] Abdi FF, Berglund SP. Recent developments in complex metal oxide photoelectrodes. J Phys D: Appl Phys 2017;50:193002.

[4] Khaselev O, Bansal A, Turner JA. High-efficiency integrated multijunction photovoltaic/electrolysis systems for hydrogen production. Int J Hydrogen Energy 2001;26:127.

[5] Chen Y, Feng X, Liu Y, Guan X, Burda C, Guo L. Metal oxide-based tandem cells for self-biased photoelectrochemical water splitting. ACS Energy Lett 2020;5(3):844–66.

[6] M Tri NL, Thuan DV, Cam NTD, Tahtamouni TA, Pham TD, Duc DS, et al. The advanced photocatalytic performance of V doped CuWO4 for water splitting to produce hydrogen. Int J Hydr En 2020;45(36):18186–94.

[7] Ahmed M, Dincer I. A review on photoelectrochemical hydrogen production systems: challenges and future directions. Int J Hydr En 2019;44(5):2474–25078.

[8] Bozheyev F, Xi F, Plate P, Dittrich T, Fiechter S, Ellmer K. Efficient charge transfer at a homogeneously distributed (NH4)2Mo3S13/WSe2 heterojunction for solar hydrogen evolution. J Mater Chem A 2019;7:10769–80.

[9] McDonald KJ, Choi K-S. A new electrochemical synthesis route for a BiOI electrode and its conversion to a highly efficient porous BiVO4 photoanode for solar water oxidation. Energy Environ Sci 2012;5:8553–7.

[10] Kim TW, Choi K-S. Nanoporous BiVO4 photoanodes with dual-layer oxygen evolution catalysts for solar water splitting. Science 2014;343:990–4.

[11] Pihosh Y, Turkevych I, Mawatari K, Uemura J, Kazoe Y, Kosar S, et al. Photocatalytic generation of hydrogen by core-shell WO3/BiVO4 nanorods with ultimate water splitting efficiency. Sci Rep 2015;5:1–10. 11141.

[12] Xiao S, Hu C, Lin H, Meng X, Bai Y, Zhang T, et al. Integration of inverse nanocone array based bismuth vanadate photoanodes and bandgap-tunable perovskite solar cells for efficient self-powered solar water splitting. J Mater Chem A 2017;5:19091–7.

[13] Seitz LC, Chen Z, Forman AJ, Pinaud BA, Benck JD, Jaramillo TF. Modeling practical performance limits of photoelectrochemical water splitting based on the current state of materials research. ChemSusChem 2014;7:1372–85.

[14] An X, Lan H, Liu R, Liu H, Qu J. Light absorption modulation of novel Fe2TiO5 inverse opals for photoelectrochemical water splitting. New J Chem 2017;41:7966–71.

[15] Khader MM, Saleh MM, El-Naggar ME. Photoelectrochemical characteristics of ferric tungstate. J Solid State Electrochem 1998;2:170–5.

[16] Yan Q, Li G, Newhouse PF, Yu J, Persson KA, Gregoire JM, et al. Mn2V2O7: an earth abundant light absorber for solar water splitting. Adv. Energy Mater 2015;5:1401840.

[17] Feng K, Akinoglu EM, Bozheyev F, Guo L, Jin M, Wang X, et al. Magnetron sputtered copper bismuth oxide photocathodes for solar water reduction. J Phys D Appl Phys 2020;53(49):495501. https://doi.org/10.1088/1361-6463/abaf25.

[18] Hosogi Y, Tanabe K, Kato H, Kobayashi H, Kudo A. Energy structure and photocatalytic activity of niobates and tantalates containing Sn(II) with a 5s² electron configuration. Chem Lett 2004;33:28.

[19] Noureldine D, Takanabe K. State-of-the-art Sn²⁺-based ternary oxides as photocatalysts for water splitting: electronic structures and optoelectronic properties. Catal Sci Technol 2016;6:7656.

[20] Jeitschko W, Sleight AW. Synthesis, properties and crystal structure of β-SnWO4. Acta Crystallogr Sect B: Struct Crystallogr Cryst Chem 1972;28:3174–8.

[21] Ziani A, Harb M, Noureldine D, Takanabe K. UV-Vis optoelectronic properties of α-SnWO4: a comparative experimental and density functional theory based study. Apl Mater 2015;3:096101.

[22] Kuzmin A, Anspoks A, Kalinko A, Timoshenko J, Kalendarev R. External pressure and composition effectson the atomic and electronic structure of SnWO4. Sol Energy Mater Sol Cells 2015;143:627–34.

[23] Su Y, Hou L, Du C, Peng L, Guan K, Wang X. Rapid synthesis of Zn²⁺ doped SnWO4 nanowires with the aim of exploring doping effects on highly enhanced visible photocatalytic activities. RSC Adv 2012;2:6266–73.

[24] Cho I-S, Kwak CH, Kim DW, Lee S, Hong KS. Photophysical, Photoelectrochemical, and photocatalytic properties of novel SnWO4 oxide semiconductors with narrow band gaps. J Phys Chem C 2009;113:10647–53.

[25] Zhu Z, Sarker P, Zhao C, Zhou L, Grimm RL, Huda MN, et al. Photoelectrochemical properties and behavior of α-SnWO4 photoanodes synthesized by hydrothermal conversion of WO3 films. ACS Appl Mater Interfaces 2017;9:1459–70.

[26] Hayashi H, Katayama S, Komura T, Hinuma Y, Yokoyama T, Mibu K, et al. Discovery of a novel Sn(II)-Based oxide β-SnMoO4 for daylight-driven photocatalysis. Adv Sci 2017;4:1600246.

[27] Manjula N, Selvan G, Balu AR. Photocatalytic performance of SnO2:Mo nanopowders against the degradation of methyl orange and rhodamine B dyes under visible light irradiation. J Electron Mater 2019;48:401–8.

[28] Zheng H, Zhang H, Fan Y, Ju G, Zhao H, Fang J, et al. A novel Mo-based oxide β-SnMoO4 as anode for lithium ion battery. Chin Chem Lett 2019;31(1):210–6.

[29] Bozheyev F, Akinoglu EM, Wu L, Lu H, Nemkayeva R, Xue Y, et al. Band gap optimization of tin tungstate thin films for solar water oxidation. Int. J. Hydr. En 2020;45(15):8676–85.

[30] Berry FJ, Hallett C, Loretto MH. An electron microscopy investigation of tin-molybdenum oxides. J Solid State Chem 1985;58:176–80.

[31] Smith DJ, Freeman LA, Berry FJ, Hallett C. Microstructural investigations of tin-molybdenum oxides by high-resolution electron microscopy. J Solid State Chem 1985;58:342–9.

[32] Gong J, Wang X, Fan X, Dai R, Wang Z, Zhang Z, et al. Temperature dependent optical properties of SnO2 film study by ellipsometry. Opt Mater Express 2019;9(9):3691–9.

[33] Bozheyev F, Xi F, I Ahmet , Höhn C, Ellmer K. Evaluation of Pt, Rh, SnO2, (NH4)2Mo3S13, BaSO4 protection coatings on WSe2 photocathodes for solar hydrogen evolution. Int J Hydr En 2020;45(38):19112—20.

[34] Zhou W, Liu Y, Yang Y, Wu P. Band gap engineering of SnO2 by epitaxial strain: experimental and theoretical investigations. J Phys Chem C 2014;118(12):6448—53.

[35] Chang X, Wu X, Guo Y, Zhao Y, Zheng J, Li X. SnSO$_4$ modified ZnO nanostructure for highly sensitive and selective formaldehyde detection. Sensor Actuator B 2018;255:1153—9.

[36] Yue L, Pu H, Pang S, Li H, Zhang Q. Top-gate LZTO thin-film transistors with PMMA gate insulator by solution process. Europhys Lett 2012;97:67006.

[37] Yang J, Yang Z, Meng T, Han Y, Wang X, Zhang Q. Effects of silicon doping on the performance of tin oxide thin film transistors. Phys Status Solidi A 2016;213:1010—5.

[38] Luo YR. Comprehensive handbook of chemical bond energies. Boca Raton, FL: CRC Press; 2007.